Graphene-intercalated Fe_2O_3/TiO_2 heterojunctions for efficient photoelectrolysis of water

A. Kaouk,[1] T.-P. Ruoko,[1,2] Y. Gönüllü,[1] K. Kaunisto,[2] A. Mettenbörger,[1] E. Gurevich,[3] H. Lemmetyinen,[2] A. Ostendorf,[3] S. Mathur[1]*

1 - Institute of Inorganic Chemistry, University of Cologne, Cologne 50939, Germany

2 - Department of Chemistry and Bioengineering, Tampere University of Technology, Tampere 33710, Finland

3 - Lehrstuhl für Laseranwendungstechnik, Ruhr-Universität Bochum, Bochum 44801, Germany

**Contact:* sanjay.mathur@uni-koeln.de

Abstract

Interfacial modification of α-Fe_2O_3/TiO_2 multilayer photoanodes by intercalating few-layer graphene (FLG) was found to improve water splitting efficiency due to superior transport properties, when compared to individual iron and titanium oxides and heterojunctions thereof. Both metal oxides and graphene sheets were grown by plasma-enhanced chemical vapor deposition. Compared to the onset potential achieved for α-Fe_2O_3 films (1 V vs RHE), the α-Fe_2O_3/TiO_2 bilayer structure yielded a better onset potential (0.3V vs. RHE). Heterojunctioned bilayers exhibited a higher photocurrent density (0.32 mA/cm2 at 1.23 V vs. RHE) than the single α-Fe_2O_3 layer (0.22 mA/cm2 at 1.23 V vs. RHE), indicating more efficient light harvesting and higher concentration of photogenerated charge carriers. For more efficient charge transport at the interface, a few layer graphene sheet was intercalated into the α-Fe_2O_3/TiO_2 interface, which substantially increased the photocurrent density to 0.85 mA/cm2 (1.23 V vs RHE) and shifted the onset potential (0.25 V vs. RHE). Ultrafast transient absorption spectroscopy studies indicated that the incorporation of FLG between the α-Fe_2O_3 and TiO_2 layers resulted in reduced recombination in the α-Fe_2O_3 layer. The results showed that graphene intercalation

improved the charge separation and the photocurrent density of the FTO/α-Fe_2O_3/FLG/TiO_2 system.

Introduction

In the on-going quest for clean and sustainable energy sources, the production of hydrogen through photochemical water splitting offer a promising solution to suppress the carbon footprint and emission of greenhouse gases.[1,2]

Transition metal oxides such as α-Fe_2O_3 and TiO_2 are favourable candidates that provide intrinsic advantages in terms of high photo-stability and sufficient mobility of charge carriers besides their earth-abundance.[3] Despite these advantages, no commercially viable material exists that would enable to maintain the proposed minimum 10 % requirement for solar-to-hydrogen fuel efficiency (STH).[4] The wide band gap of TiO_2 (anatase 3.2 eV and rutile 3.0 eV) limits it's usage in solar hydrogen production under visible light illumination. As TiO_2 is photoactive largely in the UV spectral region, only a small portion (4%) of the solar spectrum can be utilized for photocatalytic processes.[5] In the case of hematite (α-Fe_2O_3), its suitable band gap (~2.0–2.2 eV) allows harvesting a significant portion of the solar spectrum. Moreover, hematite has a valence band edge which is favourable for water oxidation reaction.[4] Although hematite yields theoretically a 20% STH conversion efficiency for water splitting,[5] high STH values have not been reached due to a combination of a relatively long light penetration depth (ca. 100 nm at λ = 500 nm) and a short hole diffusion length (2–20 nm).[6,7]. As a result, photo-generated holes that are originated deep in the material cannot reach the surface and are mostly lost in the recombination processes. In the search for strategies enabling an enhancement of the photo-electrochemical properties of TiO_2, doping with different 3d transition elements (such as Fe, V,[8] Cr,[9] Mn,[10] Cu[11]) is a promising approach to increase the visible light activity.[12-15] In the case of hematite, it has been reported that the dendritic α-Fe_2O_3 films prepared by atmospheric pressure chemical vapour deposition (AP-CVD) yielded enhanced plateau photocurrents for water oxidation due to the generation of photoholes at short distances from the semiconductor liquid interface.[16] We have previously reported that hydrogen plasma treatment of hematite films is a simple and effective strategy for modifying the existing material to improve significantly the band edge positions and photo-electrochemical (PEC) performance.[17] Sharma et al. have shown that producing multilayered TiO_2/α-Fe_2O_3 electrodes through a sol-gel process yielded approximately a 10-fold improvement in photocurrent density over a single layer electrode.[18] However, depositing a multilayered

structure with a liquid phase process creates more interfaces between the layers, resulting in recombination centers and traps for the charge carriers, which is detrimental for electron transport. Gas phase processes are used to limit the effect of interfacial interactions. Plasma enhanced chemical vapour deposition (PE-CVD) of dense layers decreases the interfacial surface area, thus improving electron mobility in multilayer systems.'[19,20] Despite the enhancement in metal oxide interfacial interactions, gas phase depositions are still limited by surface trap states and interfacial charge carrier recombination. To overcome these setbacks, charge carrier recombination in the metal oxide interface should be limited. In this context, it has been reported that a graphene sheet between two layers could improve the electron transfer.[21]

In this study, we report on α-Fe_2O_3/TiO_2 multilayered structures for water splitting applications. The interface of α-Fe_2O_3/TiO_2 was modified by intercalating a sheet of "few layer graphene". Few layer graphene, α-Fe_2O_3 and TiO_2 films were deposited by PE-CVD in order to obtain sharp interfaces and dense layers with superior interfacial properties. The α-Fe_2O_3/TiO_2 bilayer electrode exhibited a better onset potential (0.3 V vs RHE), defined as the potential were photocurrent density crosses 0 mA/cm^2, than an electrode having a single α-Fe_2O_3 layer (1 V vs RHE), whereas the highest photocurrent density (approximately 1 mA/cm^2 at 1.23 V vs RHE) was generated by the α-Fe_2O_3/FLG/TiO_2 electrode. Ultrafast transient absorption spectroscopy (TAS) studies were performed under water splitting conditions to gain insight into the effects that the layering resulted in. It was observed that the graphene layer reduced ps–ns timescale recombination in the hematite layer, indicative of graphene mediated hole transfer from α-Fe_2O_3 to TiO_2. On the other hand, the α-Fe_2O_3/TiO_2 bilayer electrode exhibited faster recombination than the single α-Fe_2O_3 layer due to unfavourable band alignment of the materials. Thus, the improved onset potential and photocurrent of the bilayer system is presumably due to the simultaneous excitation of both materials.

Experimental Section

Metal Oxide Deposition

Hematite films were deposited by radio frequency plasma enhanced chemical vapour deposition (PE-CVD) onto FTO substrates using iron pentacarbonyl ($Fe(CO)_5$) as the Fe source and pure oxygen gas as the O source, as reported elsewhere.[13,22] TiO_2 films were deposited via PECVD onto FTO substrates (as reference) and onto the graphene or hematite coated substrate by using titanium isopropoxide as a precursor. The as-grown films were amorphous and were annealed for 2 h in air at 750 °C to obtain crystalline hematite films (Fe_2O_3) and 500 °C for TiO_2.

Graphene Deposition and Transfer

The copper foil substrates (Alfa Aesar, 25 µm, 99.8%) were first dipped in an acetic acid bath to eliminate native oxides formed by the industrial process and storage,[23] after which the substrates were washed in water and isopropanol sonic bathes consecutively. The substrates were then annealed at 700 °C under vacuum to increase the grain size of the polycrystalline copper.

Treated copper substrates were used for hydrogen free PE-CVD deposition of graphene (Plasma Electronic). The substrates were placed in the PE-CVD chamber under a pressure of 2 Pa at 700 °C. The graphene deposition processes were done under a 10:1 argon to methane atmosphere with a RF power of 70 W.

A 10% PMMA (polymethylmethacrylate) in toluene solution was drop coated over the as-grown graphene layers and dried at 100 °C for 1 h[24]. The polymer covered substrate was then annealed at 180 °C for 2 h. After cooling to room temperature the copper substrate was etched in an aqueous solution of iron(III) nitrate ($Fe(NO_3)_3$) (25 w-%). The graphene-polymer sheet was washed thoroughly with deionized water and picked up from water with the preferred substrate (Si, SiO_2, Glass, FTO glass). After transfer the substrate was first dried in air and subsequently at 100 °C overnight. The polymer was finally dissolved in acetone and the graphene was rinsed in an isopropanol ultrasonic bath and blow dried.

Characterization

The powder X-ray diffraction patterns were measured (STOE-STADI MP) in reflection mode using Cu Kα (λ = 0.15406 nm) radiation. Film morphology was analysed by SEM (scanning electron microscopy, Nova Nano SEM 430 (FEI)) and absorption spectra were measured using an UV-Visible spectrophotometer (PerkinElmer Lambda 950). PEC measurements were carried out in a three electrode electrochemical cell with a 1.0 M NaOH electrolyte using a potentiostat (PAR, Model: Versa state IV, USA) and a 150 W Xenon lamp (Oriel), which was equipped with a AM1.5 filter to simulate the solar spectrum. As-grown and transferred graphene sheets were characterized using optical microscopy (Nikon Eclipse LV150) to check for the existence of layers. Layer uniformity was measured by STM (Park Systems XE-100. The number of layers and microscopic quality of the grown graphene was analysed by Raman spectroscopy (Renishaw excitation source 514 nm Ar laser). The topographic images of grown sheets were acquired by scanning electron microscopy (Carl Zeiss SMT Auriga™) and a focus ion beam (Crossbeam® FIB Workstation with Gemini® FESEM Column).

The ultrafast TAS studies were performed using the pump-probe method. The fundamental laser pulses were obtained with a Ti:Sapphire laser (Libra F, Coherent Inc., 800 nm, ~100 fs pulse width, repetition rate 1 kHz). Approximately 90 % of the fundamental beam energy was directed to an optical parametric amplifier (Topas C, Light Conversion Ltd.) to produce the excitation pump pulses at 475 nm with approximately 1 mm beam diameter at the sample, attenuated to 0.4 mJ/cm^2 with neutral density filters. The probe pulses were obtained directing the remaining fundamental laser beam energy through a motorized translational stage to a Ti:sapphire crystal for white continuum generation. The probe pulses were split into two beams for use as reference and signal beams. The measurement system (ExciPro, CDP systems) was equipped with a Si CCD for the visible part of the spectrum. A chopper synchronized with the fundamental laser pulses was used to block every second pump pulse, and the absorbance change was calculated from consecutive pulses. The absorbance changes were averaged 10,000 times per delay time. The whole measurement sequence was performed five times for each sample and averaged to minimize variations caused by excitation power fluctuations. The samples were kept in a

three electrode electrochemical cell with 0.1 M NaOH electrolyte and held at a constant bias of 1.23 V vs. the reversible hydrogen electrode to gain insight into the changes in time-resolved absorption under water splitting conditions.

Results and discussion

PE-CVD deposition of graphene

Homogeneous few layer graphene deposits with flakes of sizes over 100 μm were obtained by PECVD of 10:1 argon to methane (Figure 1a). The pre-treatment of the copper foil increased the domain sizes of the as-grown graphene layers, due to the increase in the grain size of copper (ranging from 80 μm to 100 μm).

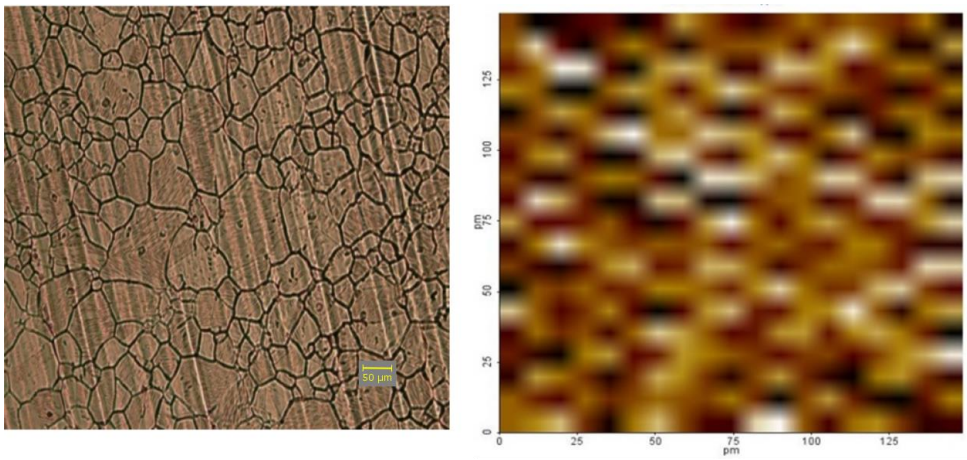

Figure 1. Optical Images of (a) as-grown graphene on copper foil and (b) STM image of as-grown graphene on copper foil (bias voltage 1.3 V, scan size 5 nm)

As-grown few layer graphene layers were characterized by STM (Figure 1b), indicating the presence of a high quality low defect graphene layer, displayed a clear hexagonal honeycomb structure.

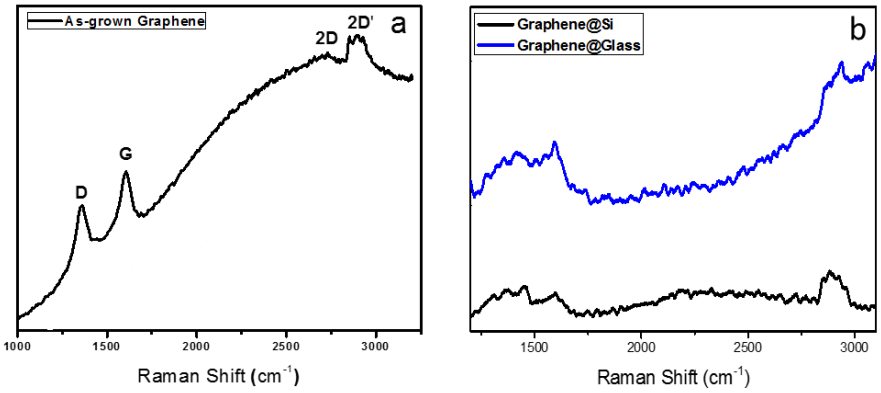

Figure 2. Raman spectra of as-grown (a) and transferred (b) graphene on copper substrate

The defect density in the synthesized graphene sheets was found to be very low ($I_D/I_G < 1$, Figure 2a). Raman spectra of the as-grown and transferred graphene layers showed 4 peaks at 1350 cm^{-1}, 1600 cm^{-1}, 2700 cm^{-1} and 2950 cm^{-1}, corresponding to the D, G, 2D, and 2D' peaks, respectively.[25] CVD-grown graphene typically exhibits two prominent peaks recognized as G and D peaks occurring at 1560 cm^{-1} and 1360 cm^{-1}, due to individual bond stretching, compressing (G band) and breathing modes of the hexagonal rings of carbon atoms (D band).[26] The D peak's intensity shows the amount of defects in the graphene structure, whereas, the ratio I_{2D}/I_G of the G peak with the 2D peak, which is the first harmonic of the D peak, shows the number of graphene layers (1- 5 layers)[27]. In all spectra, the peak appearing at 2950 cm^{-1} is due to the combination of two phonons with different momentums.[28] Raman spectra of the transferred graphene layers exhibited the same Raman shift peaks (D, G and 2D). The only difference observed was a more intense D peak, which is explained by folding and cracking of the layers during the wet transfer process, thus increasing defect density and increasing the intensity of the D peak (Figure 2b).[29]

PE-CVD deposition of MO_x and MO_x/graphene material

The crystalline phase of as deposited and annealed layers of α-Fe_2O_3 and TiO_2 were determined by X-ray diffraction analysis to be hematite and anatase, respectively (Figure 3b).

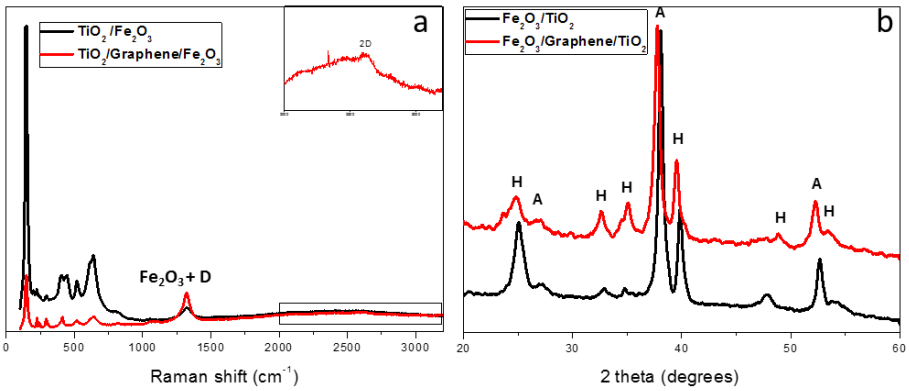

Figure 3. Raman spectra (a); X-ray diffraction patterns of hematite α-Fe_2O_3 (H), anatase TiO_2 (A) and MO_x\graphene composite material (b); Raman spectrum of SAG\Fe_2O_3 on FTO (c)

A few layer graphene sheet was transferred over a α-Fe_2O_3 thin layer, and a layer of TiO_2 was deposited over it. The pristine and composite materials were both characterized and their composition was determined with Raman spectroscopy. The 2D graphene peak can be seen at 1690 cm^{-1}, whereas the G peak is not observed due to the thick layer of metal oxide over (TiO_2) and under (α-Fe_2O_3) the graphene layer overwhelming the intensity of the peak. The wide peak at 1310 cm^{-1} is the D peak of the graphene (Figure 1a, the high D peak intensity arises from defects due to the interaction between the graphene and α-Fe_2O_3 layers.[30]

Photoelectrochemical activity of MO_x and composite materials

To overcome the drawbacks of α-Fe_2O_3, TiO_2 was deposited over it (Figure 4a), and to further enhance the interfacial properties of the multilayer system graphene was intercalated in the metal oxide interface. Graphene's zero band gap property makes it an appropriate charge collector.[31] Photocurrent density and onset voltages of all studied photoanodes under solar illumination are displayed in Table 1. All mentioned potentials are presented against the reversible hydrogen electrode (RHE). The pristine α-Fe_2O_3 and TiO_2 electrodes showed photocurrent densities of 0.22 mA/cm^2 and 0.43 mA/cm^2 at 1.23 V, respectively (Figure 5a).

Table 1. Photocurrent densities and onset potentials of fabricated electrodes

Sample	J @ 1.23 V vs. RHE ($mA.cm^{-2}$)	Onset Potential (V vs. RHE)
TiO_2	0.43	0.3
Fe_2O_3	0.22	1
Fe_2O_3/TiO_2	0.32	0.3
$Graphene/Fe_2O_3/TiO_2$	0.67	0.75
$Fe_2O_3/Graphene/TiO_2$	0.85	0.3

Further enhancement of the photo electrochemical properties was achieved by depositing a layer of TiO_2 over pristine α-Fe_2O_3. This resulted in an onset potential of 0.3 V and an increase in the photocurrent density (0.32 mA/cm^2 at 1.23 V) with respect to the pristine α-Fe_2O_3 electrode. The enhancement in onset potential is due to the favourable conduction band edge alignment of TiO_2 and α-Fe_2O_3, where photoelectrons generated in TiO_2 are injected to the conduction band of α-Fe_2O_3 due to its lower energy, leaving holes in the valence band of TiO_2 (Figure 4).[32] With increased bias voltages photoholes generated in the α-Fe_2O_3 layer attain enough energy to possibly tunnel through the TiO_2 defect states, resulting in a rise in the level of photocurrent density of the double layer α-Fe_2O_3/TiO_2 electrode.

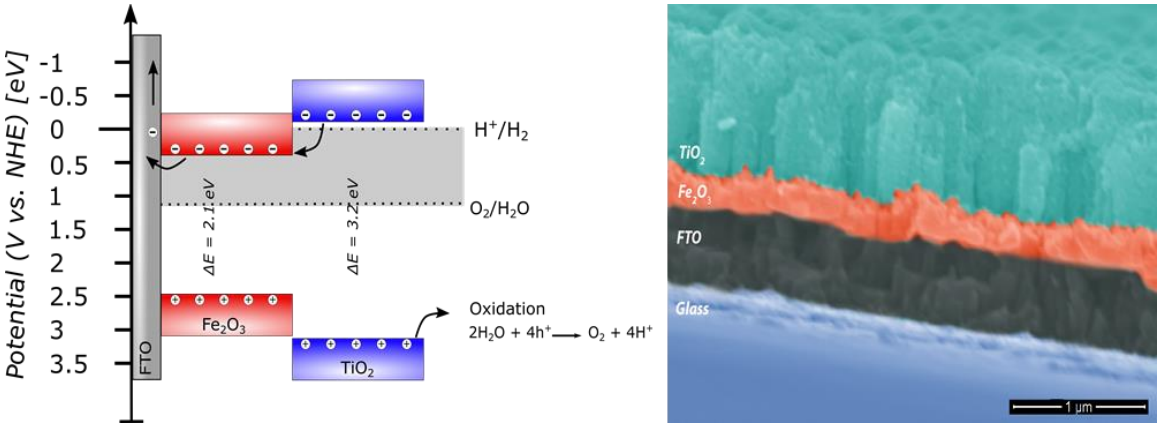

Figure 4. Schematic band edge structure of α-Fe_2O_3/TiO_2 bilayer with the redox potentials of water

Photocurrent density was further enhanced by intercalating a few layer graphene sheet between the α-Fe_2O_3 and TiO_2 layers (Figure 4b), the intercalated graphene layer cannot

be seen in the cross-section image of the multilayer, due to its thickness (1-5 layers, < 1.5 nm). The α-Fe_2O_3/FLG/TiO_2 composite electrode showed more than a 2-fold enhancement in photocurrent density over the α-Fe_2O_3/TiO_2 composite electrode (0.85 and 0.32 mA/cm^2 at 1.23 V, respectively) while enhancing the onset potential to 0.25 V (Table 1). The apparent enhancement arises from graphene's lower work function (-4.4 eV) compared to TiO_2 (-4.2 eV) making it easier for electrons to inject into the graphene layer rather than recombine at the MO_x/MO_x interface.[16] Thus, the presence of a graphene layer between the α-Fe_2O_3 and TiO_2 layers limits the electron/hole pair recombination at the α-Fe_2O_3/TiO_2 interface, which in turn increases the photocurrent density of the whole electrode. This fact is further proved in the FLG/α-Fe_2O_3/TiO_2 electrode where the measured photocurrent density (0.67 mA/cm^2 at 1.23 V) is lower than that of α-Fe_2O_3/FLG/TiO_2 (Figure 5b). This difference shows the role of the conductive band alignment in multi-layered systems (Figure 4), making the α-Fe_2O_3/TiO_2 interface the optimal place for a layer of graphene to obtain the desired enhancing effect on the performance of the electrode.

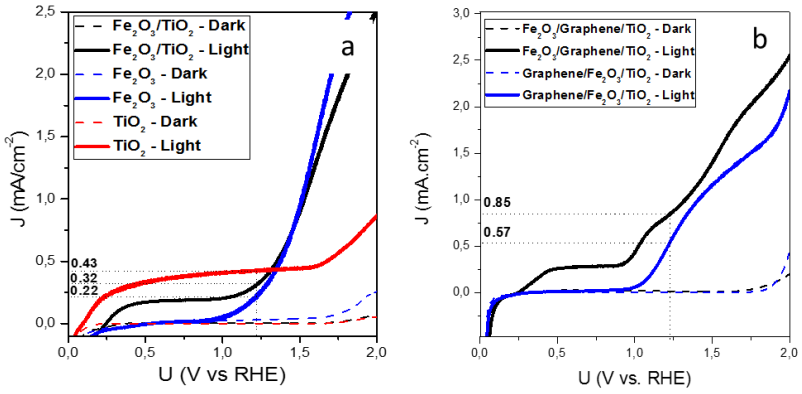

Figure 5. Photocurrent densities under dark and light conditions of (a) α-Fe_2O_3, TiO_2 and α-Fe_2O_3/TiO_2, (b)SAG/Fe_2O_3 composite, (c) Fe_2O_3/graphene/TiO_2 multilayer system

Transient absorption spectroscopy

Ultrafast transient absorption spectroscopy was used to study the effects that lead to the increased photocurrent. The excitation wavelength (475 nm) was chosen to selectively excite hematite in the multilayer systems in water splitting conditions. Thus, the decay of the transient absorption reflects the recombination and charge separation efficiencies

within the hematite layer in different samples. The normalized transient decays of the studied samples at a probe wavelength of 650 nm (Figure 6), attributed to kinetics of photogenerated charge carriers in the ps time domain and holes on longer timescales.[33,35]

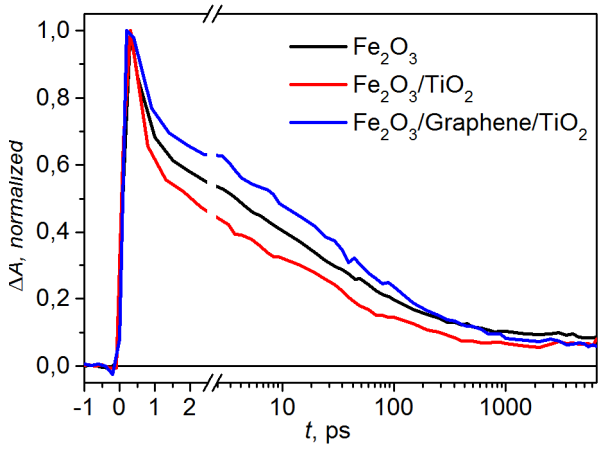

Figure 6. Picosencond to nanosecond transient absorption decays probed at 650 nm for α-Fe_2O_3, α-Fe_2O_3/TiO_2 and α-Fe_2O_3/Graphene/TiO_2.

The TAS decay in the ps timescale is attributed to primary recombination processes, as indicated by similar decay dynamics up to 1 ps for all samples. On the other hand, the longer timescale decay is a mixture of electron-hole recombination, electron extraction and long-lived hole signal. The α-Fe_2O_3/TiO_2 electrode exhibits noticeably faster primary recombination processes than the single layer α-Fe_2O_3 electrode. This is due to the fact that the valence band of TiO_2 is much lower than the valence band of α-Fe_2O_3,[36] creating a barrier for the photogenerated holes and increasing bulk recombination in the 1–1000 ps timescale. This results in a lower amount of long-lived holes in hematite that can take part in the water oxidation reaction due to the hole transfer barrier at the α-Fe_2O_3/TiO_2 interface. The higher photocurrent obtained with this sample over the single layer α-Fe_2O_3 can be explained by simultaneous excitation of both layers with simulated sunlight.

On the other hand, the α-Fe_2O_3/FLG/TiO_2 layer exhibits noticeably reduced recombination in the 1–1000 ps timescale. This is due to the fact that the photogenerated holes in hematite can now be transferred to the graphene layer, reducing recombination within the hematite layer and the interface between the metal oxide layers, thus allowing a greater number of photogenerated electrons to be conducted to the external circuit. The holes in graphene can

recombine with photogenerated electrons from TiO_2, increasing the photohole lifetime within the titania layer. This explains the higher photocurrent at low bias voltages with this sample when compared with the α-Fe_2O_3/TiO_2 double layer.

Conclusion

PE-CVD α-Fe_2O_3/TiO_2 bilayer photoanodes were modified through intercalation of few layer graphene. The observed enhancement in photocurrent suggests that heterointerface α-Fe_2O_3/FLG/TiO_2 influences the band line-up, which is attributed primarily to modulation of dislocation density and charge carrier generation/recombination rates.

The α-Fe_2O_3/TiO_2 bilayer electrode exhibited enhanced PEC responses in terms of a lower onset potential and a higher photocurrent density when compared to the single layer α-Fe_2O_3 electrode. The incorporation of a graphene layer between the α-Fe_2O_3/TiO_2 double layer and the FTO substrate resulted in a doubling of the photocurrent, but lead to a loss of the synergistic effect between the two active metal oxide layers probably due to the change of band-alignment from staggered to broken bandgap. However, intercalating the graphene between the two active metal oxide layers resulted in an overall higher photocurrent, while retaining the enhanced onset potential of the double layer electrode. This enhancement was observed to be due to either the passivation of the oxide defect states or enhancement of the charge transfer between the two oxide layers. In conclusion, the results presented in this study illustrate the importance of interfacial modification of metal oxide photoanodes, resulting in greatly increased onset voltages and photocurrents that can be adapted to a broad range of metal oxide based systems.

Acknowledgments

The work was financially supported by SOLAROGENIX, Project (EC-FP7-Grant Agreement No. 214281) and the University of Cologne. AK and SM are thankful to the Lebanese National Council for Scientific Research for providing a fellowship to Mr. Ali Kaouk. The authors are thankful to Dr.-Ing. Konstantinos Nalpantidis for Raman measurement, and Mr. Ashish Lepcha for XRD measurement.

References

1 R. Dholam, N. Patel, A. Santini and A. Miotello, Int. J. Hydrogen Energy, 2010, 35, 9581.

2 A. Fujishima, Nature, 1972, 238, 37–38.

3 R. Dholam, N. Patel and A. Miotello, Int. J. Hydrogen Energy, 2011, 36, 6519.

4 A. J. Cowan, C. J. Barnett, S. R. Pendlebury, M. Barroso, K. Sivula, M. Grätzel, J. R. Durrant and D. R. Klug, J. Am. Chem. Soc., 2011, 133, 10134.

5 I. Cesar, K. Sivula, A. Kay, R. Zboril and M. Gr€atzel, J. Phys. Chem. C, 2009, 113, 772.

6 M. P. Dare-Edwards, J. Goodenough, A. Hamnett and P. Trevellick, J. Chem. Soc., Faraday Trans. 1, 1983, 79, 2027.

7 R. Gardner, F. Sweett and D. Tanner, J. Phys. Chem. Solids, 1963, 24, 1183.

8 R. Dholam, N. Patel and A. Miotello, Int. J. Hydrogen Energy, 2011, 35(11), 6519.

9 R. Dholam, N. Patel and A. Miotello, Int. J. Hydrogen Energy, 2009, 34(13), 5337.

10 K. Umar, M. M. Haque, M. Muneer, T. Harada and M. Matsumura, J. Alloys Compd., 2013, 578(25), 431–438.

11 C. Wang, Q. Hu, J. Huang, C. Zhu, Z. Deng, H. Shi, L. Wu, Z. Liu and Y. Cao, Appl. Surf. Sci., 2014, 292(15), 161.

12 Z. Fujishima and D. Tryk, Surf. Sci. Rep., 2008, 63, 515.

13 T. Choi and M. Hoffmann, J. Phys. Chem., 1994, 84, 13669.

14 J. Zhu, Appl. Catal., B, 2006, 62, 329.

15 M. Khan, S. Woo and O. Yang, Int. J. Hydrogen Energy, 2008, 33, 5345.

16 A. Kay, I. Cesar and M. Grätzel, J. Am. Chem. Soc., 2006, 128, 15714.

17 A. Mettenbörger, T. Singh, A. P. Singh, T. T. Järvi, M. Moseler, M. Valldor and S. Mathur, Int. J. Hydrogen Energy, 2014, 39, 4828.

18 P. Sharma, P. Anjana Solanki, R. Shrivastav, S. Dass and V. R. Satsangi, J. Solid State Electrochem., 2012, 16, 1305.

19 M. Liu, M. Johnston and H. Snaith, Nature, 2013, 501, 395.

20 M. Wang, M. Pyeon, Y. Gönüllü, A. Kaouk, S. Shen, L. Guo and S. Mathur, Nanoscale, 2015, 7, 10094.

21 J. Wang, et al., Nano Lett., 2014, 14(2), 724.

22 A. Singh, A. Mettenbörger, P. Golus and S. Mathur, Int. J. Hydrogen Energy, 2012, 37, 13983–13988.

23 M. Chhowalla, J. Mater. Chem., 2011, 21, 3324.

24 L. Colombo and R. Ruoff, Nano Lett., 2009, 9, 4359.

25 M. Dresselhaus, L. Malard, M. Pimenta and G. Dresselhaus, Phys. Rep., 2009, 473(5–6), 51.

26 A. C. Ferrari, J. C. Meyer, V. Scardaci, C. Casiraghi, M. Lazzeri, F. Mauri, S. Piscanec, D. Jiang, K. S. Novoselov, S. Roth and A. K. Geim, Phys. Rev. Lett., 2006, 97(18), 187401.

27 M. Pimenta, G. Dresselhaus, M. Dresselhaus, L. Cancado, A. Jorio and R. Saito, Phys. Chem. Chem. Phys., 2007, 9(11), 1276.

28 Z. Ni, T. Yu, Z. Luo, Y. Wang, L. Liu, C. Wong, J. Miao, W. Huang and Z. Shen, ACS Nano, 2009, 3, 569.

29 X. Liang, B. A. Sperling, I. Calizo, G. Cheng, C. A. Hacker, Q. Zhang, Y. Obeng, K. Yan, H. Peng, Q. Li, X. Zhu, H. Yuan, A. R. Hight Walker, Z. Liu, L. Peng and C. Richter, ACS Nano, 2011, 5(11), 9144.

30 M. Khenfouch, et al., Opt. Mater., 2013, 36, 27.

31 R. Czerw, B. Foley, D. Tekleab, A. Rubio, P. Ajayan and D. Carroll, Phys. Rev. B: Condens. Matter Mater. Phys., 2002, 66(3), 033408.

32 S. Choudhary, S. Upadhyay, P. Kumar, N. Singh, V. R. Satsangi, R. Shrivastav and S. Dass, Int. J. Hydrogen Energy, 2012, 37, 18712.

33 M. Barroso, S. Pendlebury, A. Cowan and J. Durrant, Chem. Sci., 2013, 4, 2724.

34 S. Pendlebury, X. Wang, F. le Formal, M. Cornuz, A. Kafizas, S. Tilley, M. Grätzel and J. Durrant, J. Am. Chem. Soc., 2014, 136, 9854.

35 A. Cowan, C. Barnett, S. Pendlebury, M. Barroso, K. Sivula, M. Grätzel, J. Durrant and D. Klug, J. Am. Chem. Soc., 2011, 133, 10134.

36 J. Baxter, C. Richter and C. Schmuttenmaer, Annu. Rev. Phys. Chem., 2014, 65, 423.